Preparation and electrochemical characteristics of porous hollow spheres of NiO nanosheets as electrodes of supercapacitors

CrossMark

Wei Yu [a], Xinbing Jiang [a], Shujiang Ding [b,c,d,**], Ben Q. Li [e,*]

[a] The State Key Lab for Manufacturing Systems Engineering, Xi'an Jiaotong University, 710049 Xi'an, China
[b] MOE Key Laboratory for Nonequilibrium Synthesis and Modulation of Condensed Matter, School of Science, Xi'an Jiaotong University, Xi'an 710049, China
[c] Department of Applied Chemistry, School of Science, Xi'an Jiaotong University, Xi'an 710049, China
[d] State Key Laboratory for Mechanical Behavior of Materials, School of Science, Xi'an Jiaotong University, Xi'an 710049, China
[e] Department of Mechanical Engineering, University of Michigan-Dearborn, Dearborn, MI 48128, USA

HIGHLIGHTS

- Porous NiO hollow spheres were synthesized by electroless plating and calcination.
- Stable electrochemical property is ascribed to ultrathin nanosheets nanostructures.
- Specific capacitance of 600 F g^{-1} is obtained at a current density of 10 A g^{-1}.

ARTICLE INFO

ABSTRACT

Porous hollow nanospheres (or spherical shells) made of NiO nanosheets are synthesized and tested for the electrochemical performance of the electrodes made of these materials for supercapacitors. Preparation of the NiO sheet hollow spheres starts with synthesis of polystyrene nanospheres with carboxyl groups (CPS), followed by a two-step activation procedure and the subsequent nucleation and growth by electroless deposition of Ni on the CPS core to obtain CPS@Ni core–shell nanoparticles. The CPS core is eliminated and metallic Ni nanoshell is converted into NiO by calcinations at high temperatures. The material properties of as-prepared hollow NiO nanospheres are characterized by TEM, XRD and N_2-absorption measurements. The electrochemical characteristics of the electrodes made of these nano-structured NiO materials are determined by the CV and galvanostatic measurements. These electrochemical tests indicate that electrodes made of the NiO nanosheet hollow spheres exhibit an improved reversible capacitance of 600 F g^{-1} after 1000 cycles at a high current density of 10 A g^{-1}. It is believed that the good electrochemical performance of these electrodes is attributed to the improved OH$^-$ transport in the porous network structures associated with the hollow spheres of randomly oriented NiO nanosheets.

© 2014 Published by Elsevier B.V.

1. Introduction

As emerging energy storage devices, electrochemical super-capacitors have attracted much attention, because of their super energy storage characteristics, such as the high power density, long lifecycle, low maintenance cost, broader working temperature and shorter charging time [1,2]. These devices are often used as power storage sources to meet the energy needs for high power applications such as electric vehicles, memory back-up and aerospace equipment. Supercapacitors in general are classified as electric double-layer capacitors and pseudocapacitors. The former stores the energy by building up electric charges at the two sides of an electric double layer, while the latter (i.e. pseudocapacitors) is based on the fast, reversible redox reactions at the electrode/electrolyte interface to achieve high power storage.

Metal oxides [3–12] and conducting polymers [13,14], have been explored recently for pseudocapacitor applications. Among the materials studied, nickel oxides represent a promising choice,

* Corresponding author.
** Corresponding author. MOE Key Laboratory for Nonequilibrium Synthesis and Modulation of Condensed Matter, School of Science, Xi'an Jiaotong University, Xi'an 710049, China.
E-mail addresses: dingsj@mail.xjtu.edu.cn (S. Ding), benqli@umich.edu (B.Q. Li).

owing to its high specific capacity, low cost, easy preparation, and environmental compatibility [15]. Practical use of nickel oxide supercapacitors, however, has been hindered by some geometric and electrical factors that impede the electronic and ion transport during power cycling. Energy storage capacity of supercapacitors is affected by various properties of the electrodes, such as porous network, specific surface area, morphology and electrical conductivity. A viable approach for improved electrical capacitance is to construct the electrode from nanostructured materials. The reported capacitance of the electrodes made of nanostructured NiO materials has reached a value of 128–405 F g^{-1} [16–19]. Though impressive, this is still far from the theoretical value of 2573 F g^{-1} [18], suggesting the low electrochemical utilization of nickel oxide materials.

The specific capacitance of a NiO electrode hinges strongly on the proper pore structures in the electrode to ensure good mechanical and electric contact for high power density during charging/discharging operations. Through years of research, nanotechnology has now advanced to the state at which porous nanostructure network may be designed and engineered for better pseudocapacitive performance. Indeed, different synthesis procedures have been reported for nanostructured materials for supercapacitors, including electrodeposition [11], the anodically potentiostatic deposition [20], chemical deposition [21], wet-chemistry route [22], and solvothermal method [23]. Structures of 0D to 3D have been successfully synthesized, including nanoparticles (0D) [24], nanotubes, nanorings, nanowires and nanorods (1D) [11,25–28], nanosheets (2D) [12,29], and nanosheets arrays grown on substrates (3D) [19]. Electrodes made of these nanostructured materials have met with different degrees of success.

This paper presents a study on the synthesis and electrochemical characteristics of porous hollow nanospheres (or spherical shell) of NiO nanosheets as electrode for supercapacitors. Since fast electron and ion transport in the electrode are essential for a desired electrochemical performance, a nanostructured porous spherical shell should possess a larger specific surface area than either a solid sphere or a solid spherical shell, and hence permits better mechanical and electrical contact with electrolytes for improved electron and ion transport. The porous hollow spheres, whose porous structure is formed by randomly organized ultrathin NiO nanosheet network, are produced by first synthesizing a CPS@Ni core–shell nanostructure with a CPS (polystyrene with carboxyl groups) template, followed by high-temperature oxidation to remove the CPS core. The nanostructured porous hollow NiO spheres so obtained appear to have a proper porosity with a high specific surface area for good pseudocapacitive behavior. Electrochemical tests were performed on the electrodes made of the porous hollow spheres structured with a NiO nanosheet network. The porous NiO spherical shell nanostructure formed by loosely cross-linked ultrathin nanosheets is benefit to the sufficient electrochemical accessibility of electrolyte to the electroactive sites for Faradaic energy storage, resulting in more efficient ion transport and probably improved capacity for ion storage as well. One additional advantage of this nanostructure is that the stress, originating from redox process, could be effectively relieved by interspaces between the nanosheets, thereby ameliorating the charge–discharge cycling performance [5,17,30,31].

2. Experimental section

2.1. Materials

Acrylic acid (Tianjin Fu Chen Chemical Reagents Factory, 98%), ammonium persulfate (APS, Tianjin Sheng Ao Chemical Reagent Co., LTD, 98%), stannous chloride (Aladdin Chemistry Co. Ltd, 98%), palladium chloride (Aladdin Chemistry Co. Ltd), nickel chloride (Aladdin Chemistry Co. Ltd, 99%), hydrochloride acid (Beijing Chemical works, 36%–38%), sodium hypophosphite (Tianjin Tian Li Chemical Reagent Co., LTD, 99%), ammonium chloride (Tianjin Tian Li Chemical Reagent Co., LTD, 99.5%), basic alumina (Aladdin Chemistry Co. Ltd), trisodium citrate dehydrate (Tianjin Tian Li Chemical Reagent Co., LTD, 99%) and ammonium solution (Tianjin Fu Yu Fine Chemical Co., LTD, 25%–28%) were all analytical reagent and used as received without any further purification. Styrene (analytical reagents, Tianjin Fu Chen Chemical Reagents Factory, China, 98%) was filtered through basic alumina powder. Deionized water was used as the solvent in all experiments.

2.2. Preparation of polystyrene nanospheres with carboxyl groups

The CPS (polystyrene with carboxyl groups) nanospheres were prepared by emulsifier-free emulsion polymerization reported elsewhere [32]. A volume of 6 ml Styrene monomer was charged in three-neck reaction vessel containing 200 ml deionized water. After sealed in a nitrogen atmosphere, 0.6 ml divinyl benzene and 1.6 ml of 0.24 M ammonium hydroxide were added. Then, the reactor was submerged in an oil bath. The temperature was increased to 70 °C for the decomposition of initiator, and then 2.5 ml of 0.17 M acrylic acid and 12.5 ml of 37 mM potassium persulfate solution were injected. The reaction was left to reflux for 8 h. The mixture was allowed to cool and repeatedly washed with water by centrifugation. At last, the resulting CPS nanospheres were dried at 30 °C for further use. The CPS nanospheres so obtained are negatively charged when dissolved into solution.

2.3. Preparation of NiO nanosheet hollow spheres

The CPS (50 mg) nanospheres as prepared above were dispersed into the solution of $SnCl_2$ (0.1 M) for 40 min at ambient atmosphere [33]. The mixture was centrifuged to remove redundant Sn^{2+} and redispersed in deionized water. The Sn^{2+}-sensitized PS nanospheres were dipped into a palladium chloride and hydrochloride acid (30 mM) for 30 min at 60 °C, resulting in Pd-decorated CPS nanospheres. Then the nanospheres were washed by repeated centrifuging and redispersing using deionized water. The washed particles were dispersed in 30 ml deionized water, into which were added 10 ml of the electroless deposition solution (0.126 M $NiCl_2 \cdot 6H_2O$, 0.188 M $NaH_2PO_2 \cdot H_2O$, 0.93 M NH_4Cl and 0.17 M $Na_3C_6H_5O_7 \cdot 2H_2O$) [34]. The pH value of the plating solution was adjusted to be 8.25 ± 0.05 by adding ammonium hydroxide buffer solution. The electroless plating reaction was allowed to continue for 1 h at 65 °C. The product was collected via centrifugation and washed for three cycles of centrifugation–redispersion. The as-prepared CPS@Ni core–shell composite spheres were converted into NiO hollow spheres by calcination at 400 °C for 4 h in air at a ramping rate of 2 °C min^{-1}.

2.4. Materials characterization

X-ray powder diffraction (XRD; SHIMADZU, Lab X XRD-6000) patterns were recorded on a Bruker D8 ADVANCE X-ray diffractometer at a scan rate of 0.05° s^{-1} with the 2θ range from 20° to 90°, using Cu Kα radiation. The morphology and the structure of the samples were characterized using a transmission electron microscope (TEM; JEOL, JEM-2100, 200 kV). The composites' Brunauer, Emmett, and Teller (BET; Quantachrome, ASAP 2020/2000) specific surface areas, Barrett–Joyner–Halender (BJH) pore volume, and BJH pore-size distribution were obtained from the N_2-adsorption/desorption isotherms recorded at 77 K.

3. Electrochemical measurements

The working electrode was prepared by mixing 70 wt% of the active material (NiO hollow spheres), 20 wt% of conducting agent (carbon black, super-P-Li), and 10 wt% of binder (polyvinylidene difluoride, PVDF, Aldrich). This mixture was then pressed onto the glassy carbon electrode (Aida Hengsheng Technology co. Ltd, Tianjin, China) and dried at 60 °C. The electrolyte used was a 2 M KOH aqueous solution. The electrochemical measurements of the samples was tested on a CHI 660D electrochemical workstation with cyclic voltammetry and chronopotentiometry functions using a three-electrode cell where Pt foil serves as the counter electrode and a standard calomel electrode (SCE) as the reference electrode.

4. Results and discussion

4.1. Synthesis and material characterization

4.1.1. Synthesis

Fig. 1 illustrates the synthesis steps by which a porous hollow nanosphere made of ultrathin NiO sheets is fabricated on a template of a sacrificial CPS core. The synthesis process involves a two-step activation of Pd seeds, followed by a reduction of Ni from salt solution to form a CPS@Ni core–shell structure and the subsequent removal of the PS core and oxidation of Ni shell by calcination.

The two-step activation process refers to Sn^{2+}-sensitization and Pd-activation. The CPS nanospheres with carboxyl groups (CPS) first were sensitized with Sn^{2+} absorbed onto the CPS surfaces by electrostatic interaction. Because the presence of Sn^{2+} on the CPS surface imparts a positive charge onto the nanospheres, the Sn^{2+}-sensitized CPS nanospheres are well dispersed in the solution due to electrical repulsion and, at the same time, active in attracting negatively charged ions. In a chloride acid aqueous solution, $PdCl_2$ exists in the form of $[Pd(Cl)_4]^{2-}$. Thus, by electrostatic attraction, the $[Pd(Cl)_4]^{2-}$ ions are absorbed onto the surface of the Sn^{2+}-sensitized CPS nanospheres and subsequently reduced to Pd on the surface by Sn^{2+}, according to the following red-ox reaction,

$$Sn^{2+} + Pd^{2+} \rightarrow Sn^{4+} + Pd \qquad (1)$$

It was observed during the experiment that as the reduction reaction proceeds, the color of the solution in which the sensitized CPS spheres are dispersed changes from yellow to brown, indicating the formation of Pd nanoparticles on the surface [35,36]. These metallic Pd nanoparticles act as *in-situ* catalytic sites for the

subsequent reduction of nickel from its salt solution. This two-step activation process, that is, sensitizing by $SnCl_2$ and activation by $PdCl_2$, has an advantage of avoiding the agglomeration of resulting products (i.e. CPS@Ni) during electroless nickel plating if excess catalyst ions or atoms are removed before the Pd-activated CPS templates are immersed into the plating bath [37].

With the Pd active sites present on the CPS surface, the electroless deposition of nickel starts to occur at the Pd sites according to the reaction: $Pd + Ni^{2+} \leftrightarrow Pd^{2+} + Ni$. These Ni nanoparticles, reduced by Pd from the solution, take the sites on the surface that used to be the Pd sites, and further act as nucleation sites upon which Ni nanoparticles grow by reducing Ni^{2+} ions from its salt solution according to the following reaction,

$$Ni^{2+} + 2H_2PO_2^- + 2H_2O \rightarrow Ni + 2H_2PO_3^- + H_2 + 2H^+ \qquad (2)$$
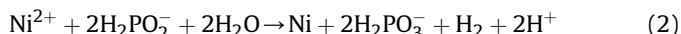
This is indicated by the color of the particle solution, which turned to black within several minutes after electroless plating starts, accompanied with the formation of H_2 bubbles.

4.2. TEM characterization

The morphologies of the nanostructured CPS@Ni core–shell composite nanospheres and of the porous hollow spheres of NiO nanosheets, prepared as discussed above, are characterized by TEM and the results are shown in Fig. 2. The CPS spheres are covered ultrathin Ni nanosheets that are randomly oriented, creating a spherical shell of large porosity. The length of nanosheets is on the order of 50 nm (Fig. 2b, c), measured as the difference between the radius of CPS sphere and the outer tip of the nanosheets, and the thickness of nanosheets is about 5 nm (Fig. 2f). Note that the condition used here produces a porous nickel shell made of thin sheets covering the CPS core. This is in contrast with the reported structures in literature where the CPS surface was coated with a solid layer of metallic nickel [38–41]. A porous nanoshell made of cross-linked thin nanosheets has an advantage of having a significantly larger surface area, which is desirable for supercapacitor applications.

After calcined in air at 400 °C for 4 h, the sacrificial CPS spheres are removed, and at the meantime, the porous Ni shell is converted into nickel oxide by oxidation. This process produces the shape-preserved NiO hollow spheres that are made of cross-linked nanosheets (see Fig. 2d, e). It is generally accepted that this kind of porous nanostructures is instrumental in increasing the contact area of NiO with the electrolyte, thereby permitting faster transport of electrolyte ions.
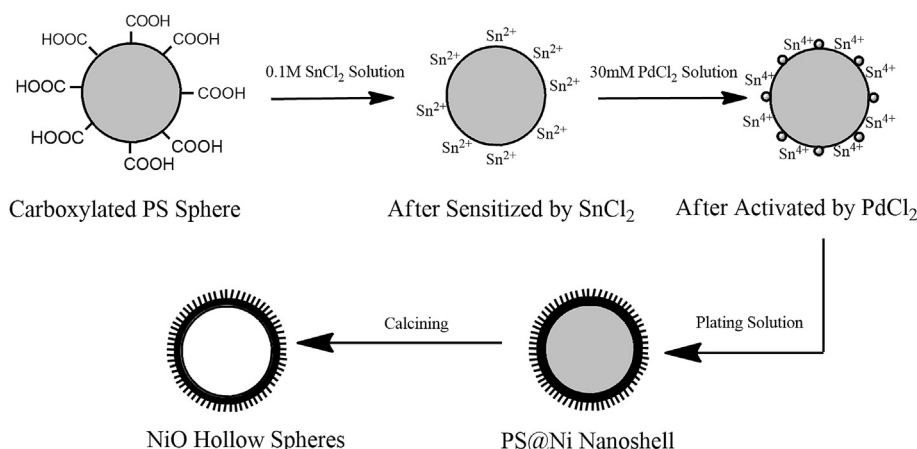

Fig. 1. Scheme for electroless deposition of Ni onto a CPS sphere and formation of a NiO nanosheet hollow sphere.
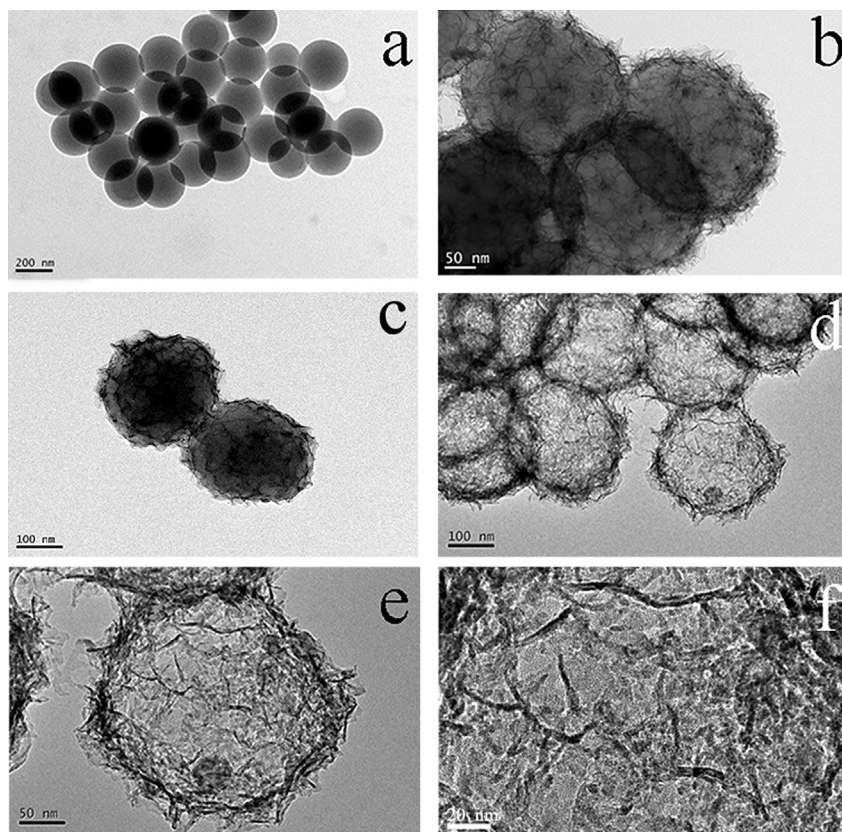
Fig. 2. TEM image of CPS(a), CPS@Ni nanoshell (b and c), (d, e and f) NiO hollow sphere.

4.3. XRD characterization

The crystal phase of as-prepared NiO samples is analyzed by the X-ray diffraction (XRD), and the results are shown in Fig. 3. The identified diffraction peaks at 37.3°, 43.4°, 63°, 75.5° and 79.5° can be assigned to (111), (200), (220), (311) and (222) lattice plane of the NiO. The diffraction peaks at 26° and 34° can be assigned to (110) and (101) lattice plane of the SnO_2. These results confirm that nickel oxide with a rocksalt structure and stannic oxide with a rutile structure had formed after calcination where the identified
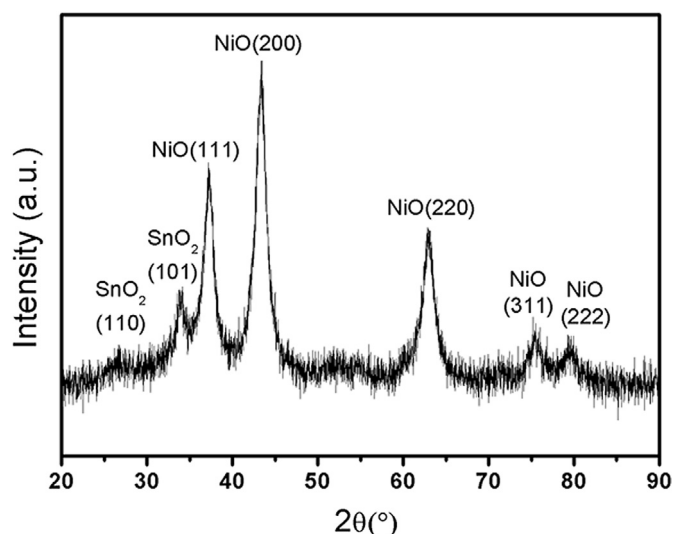
peaks confirm the cubic phase of NiO (JCPDS file no. 4-835, space group: Fm3m, $a_0 = 4.1769$ Å) and the tetragonal phase of SnO_2 (JCPDS card no. 41-1445).

Measurements were also carried out using EDX. The presence of Pd was not detected. From the measured data of EDX and XRD, the ratio of SnO_2 over NiO was found to be ~1/10.

4.4. Absorption–desorption measurements

To characterize the specific surface area associated with the porous nanostructures of the as-prepared porous hollow spheres of NiO nanosheets, nitrogen adsorption–desorption isotherm experiments were conducted. The absorption–desorption curves and the corresponding Barrett–Joyner–Halenda (BJH) pore size distribution are shown in Fig. 4. The isotherms are classified as type III, due to the slit shape channel, with a small hysteresis loop [42]. There exists a distinct hysteresis loop in the range 0.2–0.98 P/P_0 for the present nanostructures. The Brunauer–Emmett–Teller (BET) specific surface area of the NiO nanosheet hollow sphere sample is 81 $m^2 g^{-1}$. For the calculation of pore size distribution, desorption isotherm was adopted. As the NiO hollow spheres are composed of nanosheets, the shapes of the pores are narrow strips and the pore size distribution is relatively wide (see Fig. 4b). The majority of pores have a size in the range of 3–17 nm, revealing that the sample contains mesoporous structures, which is beneficial to the formation of the double electrode layer and the achievement of a maximum capacitance. The majority of the pores lie in a size range of 5–11 nm.

5. Electrochemical performance

The electrochemical performance of an electrode made of the porous hollow spheres of NiO nanosheets, as prepared above, was
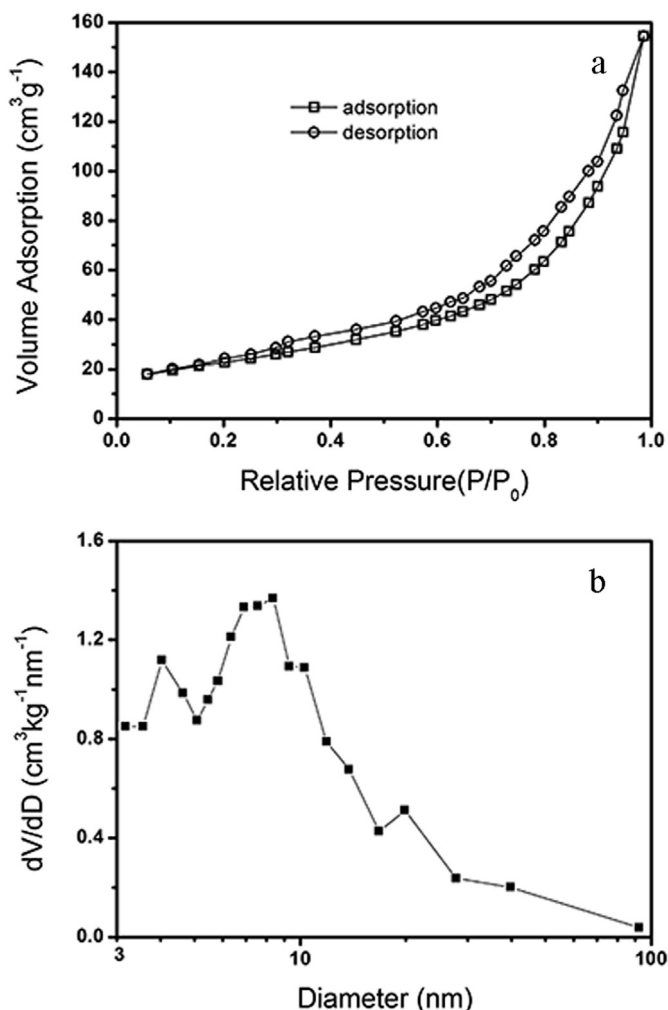

Fig. 3. XRD patterns of NiO sheet hollow spheres.

Fig. 4. Characterization of porous structures of NiO nanosheet hollow spheres: (a) Nitrogen adsorption/desorption isotherm and (b) pore size distribution calculated using the BJH method from the desorption curve.

studied using both cyclic voltammetric (CV) and galvanostatic measurements.
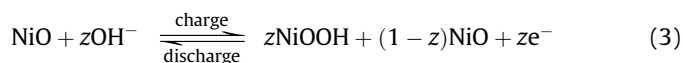
5.1. Cyclic voltammetric measurements

The CV measurements were conducted in a 2 M KOH electrolyte and a standard calomel electrode (SCE) was used as reference electrode. The cyclic voltammograms of the electrode performed at the scanning rates of 5, 10, 20, 50, 100 and 200 mV s^{-1} in a potential range of 0−0.5 V are plotted in Fig. 5a. The results show the CV curves of similar shape with an almost mirror image, which indicates the pseudocapacitance originating from the redox reaction of electrode active material. These curves are distinguished from those of a pure electric double-layer capacitor which are almost of an ideal rectangular shape. The CV curves in Fig. 5a are characterized by a distinct pair of redox peaks during the anodic and cathodic sweeps as the result of NiO being oxidized to NiOOH (charging) and of NiOOH reduced to NiO (discharging). It is known that a nickel oxide pseudocapacitor in an alkaline solution relies on charge storage in the electric double layer at the electrode/electrolyte interface and in the host material through redox reactions on the surface and hydroxyl ion diffusion [30]. The latter involves the conversion of NiO into NiOOH at the electrode/solution interface probably within several angstroms through the tunneling of

electrons supplied from the electrode [43−47]. This appears to be confirmed by the measurements.

The potentials at which the respective oxidation and reduction reactions take place are termed as oxidation potential (E_O) and reduction potential (E_R), respectively. The relevant potential parameters determined from the measurements are summarized in Table 1.

The electrochemical redox process of NiO involves the surface Faradaic reactions of Ni^{2+} to Ni^{3+} during oxidation (charging) and of Ni^{3+} to Ni^{2+} during reduction (discharging) [17,48],

$$\text{NiO} + z\text{OH}^- \xrightleftharpoons[\text{discharge}]{\text{charge}} z\text{NiOOH} + (1-z)\text{NiO} + z\text{e}^- \qquad (3)$$

where z ($z = 0-1$) represents the fraction of nickel sites involved in the electrochemical process, and reflects the material utilization of the electrode active material. As is evident from the CV curves recorded in Fig. 5a, the peaks correspond to the redox pair of Ni^{2+}/ Ni^{3+} and the redox current intensity is quite high due to an abundant surface area of NiO electrode for fast, reversible Faradaic reactions. Thus nanostructured porous spherical shells with sheet-cross-linked morphology under present study should be useful as electrode material for supercapacitors.

Detailed inspection of Fig. 5a uncovers that the cathodic sweeps of CV curves are not completely symmetric to their corresponding
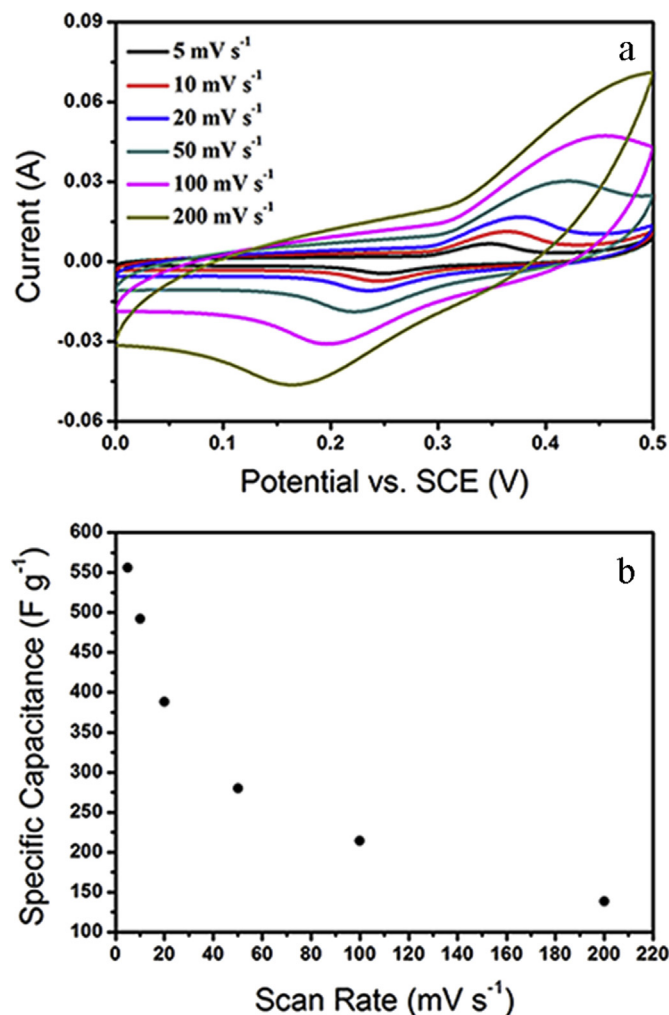

Fig. 5. (a) CV curves of NiO hollow spheres at various scan rates. (b) Average specific capacitance of NiO nanosheet hollow spheres at various scan rates.

Table 1
Oxidation potential (E_O), reduction potential (E_R), and ($E_O - E_R$) for different NiO.

Scanning rates mV s^{-1}	E_O (mV)	E_R (mV)	$E_O - E_R$ (mV)
5	348	250	98
10	364	244	120
20	376	235	141
50	421	222	199
100	455	196	259
200	499	164	335

anodic sweeps, suggesting that some electrochemical irreversibility exists in the redox process [49–51]. Pseudocapacitors involving Faradaic redox reactions have various thermodynamic and/or ion transport barriers, which prevent the ideal reversibility from being realized kinetically for the positive and negative sweeps. For instance, Ohmic loss resulting from electrolyte diffusion within the porous electrode can contribute to the kinetic irreversibility of the redox reaction [49,52]. Electrochemical reversibility is important for the performance of pseudocapacitors, as the occurrence of the irreversibility reduces the reversibly accessed active surface sites for redox reactions, resulting in power loss. The ΔE ($E_O - E_R$) value from cyclic voltammograms may be used as a measure of reversibility: a smaller value corresponds to better reversibility and *vice versa* [52]. Among the CV curves, the highest reversibility ($\Delta E = 98$ mV) occurs at a sweep rate of 5 mV s^{-1}. An increase of scan rates causes ΔE to arise and make the redox process more irreversible. This is clearly seen in the measured data in Table 1.

The specific capacitance (C) values of the samples may be estimated from the CV curves by graphically integrating the area under the $I–V$ curve and then dividing it by the sweep rate v (V s^{-1}), the mass of NiO (w) and the potential window (V_a to V_c),

$$C = \frac{1}{vw(V_a - V_c)} \int_{V_a}^{V_c} I dV \qquad (4)$$

In the above equation, I (A) is cathodic or anodic current and $\Delta V = V_a - V_c$ (V) is the applied potential window. From the CV curves in Fig. 5a, the specific capacitances of the NiO nanosheet hollow sphere electrodes are calculated to be 556, 492, 388, 280, 214 and 138.6 F g^{-1} at scan rates of 5, 10, 20, 50, 100 and 200 mV s^{-1}. The data are plotted in Fig. 5b. Clearly, the C is the largest at the scan rate of 5 mV s^{-1} and decreases in value as the scan rate increases. Indeed, it decreases significantly over a scan rate range of 5 mV s^{-1} up to 100 mV s^{-1} but the decrease slows down at a scan rate >100 mV s^{-1}. The decrease in C with increasing scan rate for NiO electrode is also observed in other electrode materials [52–54].

The effect of scan rate on pseudocapacitance may be explained by the detailed transport processes associated with the electrode kinetics. For NiO-based supercapacitors, the charge storage mechanism is due to a process of forming nickel oxyhydroxide (NiOOH) by intercalating OH$^-$ in oxide lattice [52], similar to a protonation process in Ru$_2$O$_3$ electrode [49,53,54] and thus the diffusion transport of OH$^-$ can be very important in determining pseudocapacitance. The Faradaic redox process involves electron hopping and the insertion/extraction of OH$^-$ in the NiO lattice [52–54]. Nickel ions receive or release hydroxide anions (OH$^-$) during the reduction or oxidation processes (see Eq. (3)), respectively, and the anions exchange with electrolytes and with the electrode at the interface. For a complete reduction reaction, the OH$^-$ ions must be transferred by diffusion from the electrolyte outside of the electrode (e.g., from the separator or another electrode). On the other hand, these anions (OH$^-$) need to transfer back, again by diffusion, to the electrolyte outside of the electrode during oxidation. The

porous structure of the NiO electrode facilitates the diffusion transport process. The exchange with the electrode interface involves the intercalation of OH$^-$ in the lattice of NiO [52]. These OH$^-$ transfer processes must be synchronized with the electron transport in the electrode if an optimal electrochemical performance is to be obtained. Since the OH$^-$ transfer processes are in general slow, they are unable to respond in time to the rapid change of potential (or change in electron transport) during the fast reduction and oxidation scans. Consequently, a high scan rate leads to a rapid depletion of OH$^-$ during charging (oxidation) or oversaturation of OH$^-$ during discharging (reduction) [54]. The depletion or oversaturation of OH$^-$ at the electrolyte/electrode interface makes parts of the surface of the electrode inaccessible (or inactive) at high charging–discharging rates, thereby impeding the charge transfer process and causing an increase in resistance [55,56]. By the equivalent circuit model of a pseudocapacitor, an increase in resistance leads to a drop in the pseudocapacitance of the NiO electrode [54]. On the other hand, at a slower scan rate, electron transport may be synchronized with OH transfer in rate, thereby resulting in a lower resistance or high pseudocapacitance.

A fraction of NiO sites that has participated in the surface redox reaction is related to the value of "z" in Equation (3), which may be estimated from the specific capacitance by using the expression,
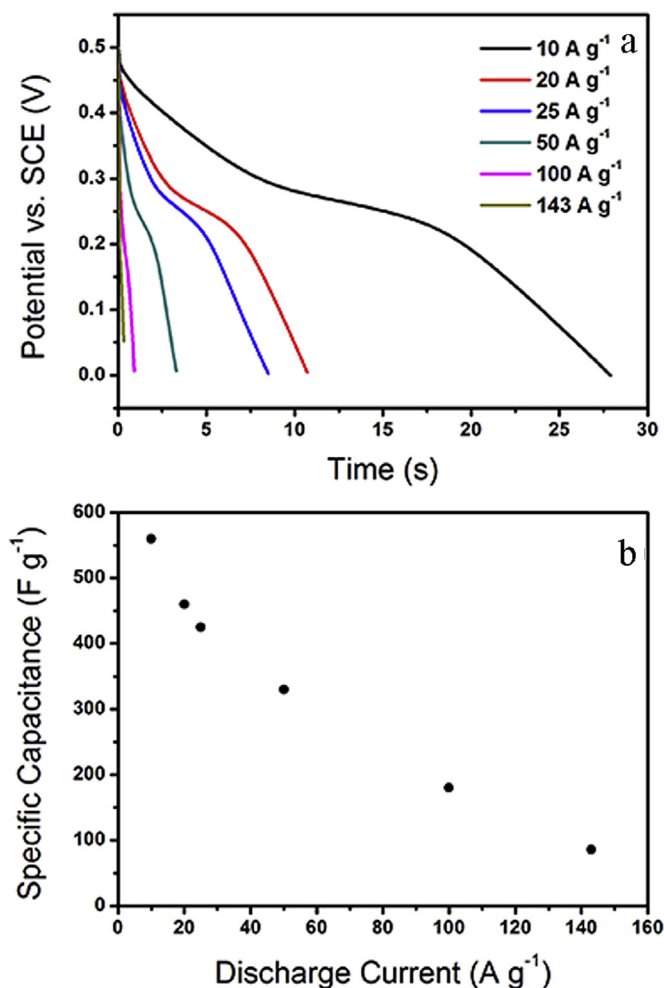
$$z = CM\Delta V/F \qquad (5)$$

Fig. 6. (a) Galvanostatic discharge curves of NiO hollow spheres at various discharge current densities. (b) Average specific capacitance of NiO hollow spheres at various discharge current densities.

With a potential window (ΔV) of 0.5 V, a molecular weight (M) of 74.692 g mol^{-1}, the Faraday constant (F, 96487 C mol^{-1}) and the calculated specific capacitance values (C) in Fig. 5b, the "z" values obtained at the sweep rate of 5, 10, 20, 50, 100 and 200 mV s^{-1} are 21.35%, 19.04%, 15.01%, 10.83%, 8.28% and 5.36%, respectively. Thus, an estimated 21.35% of sites participate in the redox reaction at a scan rate of 5 mV s^{-1}, which are significantly higher than the values reported on NiO films or similar other nano NiO structures [57]. These data suggest that within the present porous structure made of randomly oriented nanosheets, the OH$^-$ ions can move more freely in the structure for a better yield of Faradaic reaction at a slow scan rate. On the other hand, the OH$^-$ transfer becomes slow in catching up with the electron transport, resulting in the active surface area being lost at a high scan rate. For instance, at 200 mV s^{-1}, $z = 5.36\%$ or only 5.36% of the available sites participate in the redox process. This further is consistent with the picture developed from the standpoint of ion and electron transport processes discussed above.

5.2. Galvanostatic measurements

The galvanostatic charge/discharge measurements were conducted to test the electrochemical stability of the electrode made of porous hollow spheres of NiO nanosheets. The galvanostatic charge–discharge tests of NiO electrode were performed using a three-electrode cell, in which the NiO electrode, Pt foil and saturated calomel electrode were used as the working electrode, the counter and reference electrode, respectively. The electrolyte was a 2 M KOH aqueous solution. The galvanostatic charge–discharge tests of the electrode were conducted at the scanning rates of 10, 20, 25, 50, 100 and 143 A g^{-1} with a CHI 660D electrochemical workstation in the potential range of 0–0.5 V, where the active substance content was 0.7 mg. The measured data may also be used to understand the detailed pseudocapacitive behavior. The measurements were made at various current density rates and the results are shown in Fig. 6a, where the time-variation of potential during discharge is plotted as a function of discharge current.

Apparently, the nonlinear behavior of the galvanostatic charge–discharge curves further confirms the result from the CV measurements that the charge separation in the double layer and the redox process both contribute to the specific capacitance, a characteristic of pseudocapacitor. Specifically, the double layer capacitance resulting from the charge separation between the electrode/electrolyte interface is manifested by the linear relation of the galvanostatic charge/discharge curve for the range of 0–0.2 V. The slope change of the charge–discharge curve from 0.2 V to 0.5 V, on the other hand, reveals that a good portion of capacitance comes from the contribution of the redox reaction of NiO with the electrolyte.

For the galvanostatic measurements, the specific capacitance C_m (F g^{-1}) may be calculated by the following expression,

$$C_m = I \times \Delta t / (\Delta V \times m) \tag{6}$$

where I (A) is the discharge current, Δt (s) the discharge time, ΔV (V) the potential change during discharge, and m (g) the mass of the active material in the working electrode. The specific capacitance is calculated to be 560, 460, 425, 330, 180 and 85.8 F g^{-1} corresponding to the discharge currents of 10, 20, 25, 50, 100 and 143 A g^{-1}, (see Fig. 6b). The specific capacitance decreases with increasing the discharge current, which, as in the case of the CV measurements, can be fully explained by the electron and ion transport processes discussed above.

Fig. 7a shows the charge/discharge voltage profiles of the first 10 cycles taken from galvanostatic measurements. Apparently, the charging and discharging curves of the samples are not completely symmetrical, which is attributed to the kinetic irreversibility of the OH$^-$ ions on the NiO nanosheet surface during the redox reaction.

Turning to the electrochemical stability of the electrode, the specific discharge capacitance is plotted against the number of the charge/discharge cycles for up to 1000 cycles, as shown in Fig. 7b. The specific capacitance of the NiO electrode is maintained at 600 F g^{-1} even at the end of 1000 cycles, which indicates that essentially ca. 100% of their initial capacitance is retained. This suggests that the ultrathin NiO nanosheet cross-linked porous structure has a very little minimal structural modification or degradation and/or the crystallographic change during the repeated insertion/extraction of OH$^-$ ions into/from the NiO lattice of the electrode. The morphology of these porous hollow spheres of NiO nanosheets is capable of coping with the mechanical fatigue associated with the surface redox reactions, which generate and relieve stresses on the NiO lattice. It is noticed that during the first 100 cycles, the specific capacitance increased from 560 F g^{-1} to 600 F g^{-1}, which is attributed to the activation process of the NiO electroactive material.

The above CV and galvanostatic testing results suggest that these NiO hollow spheres of ultrathin nanosheets possess high quality of relatively high specific capacitances and excellent capacitance retention, and are suitable candidates for
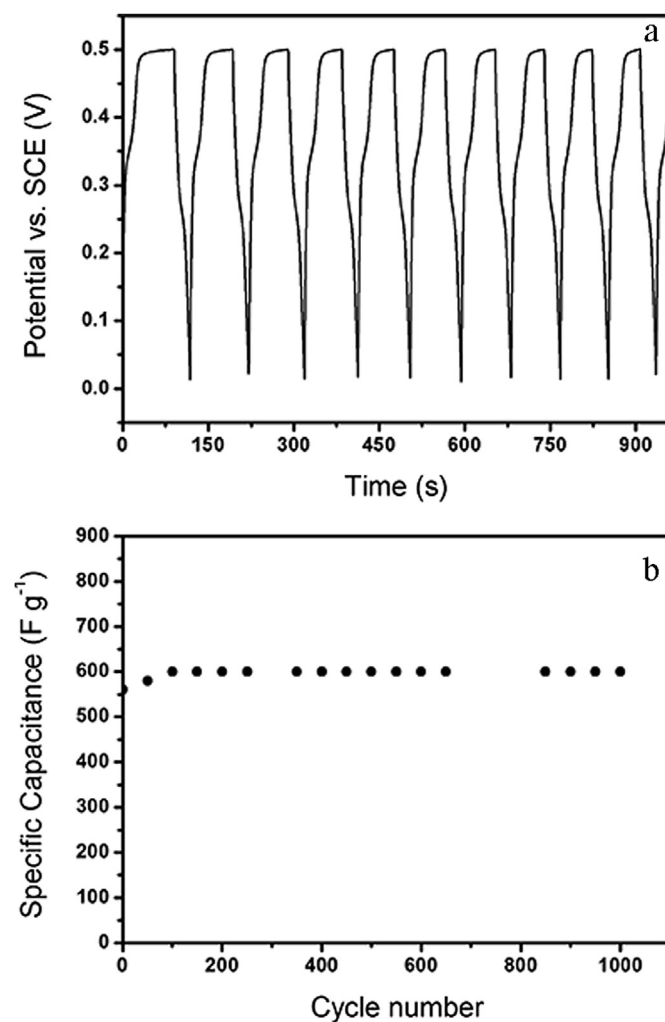

Fig. 7. (a) Galvanostatic charge and discharge voltage profiles of NiO hollow spheres at a current density of 10 A g^{-1}. (b) Average specific capacitance retention versus cycle number of NiO hollow spheres at a current density of 10 A g^{-1}.
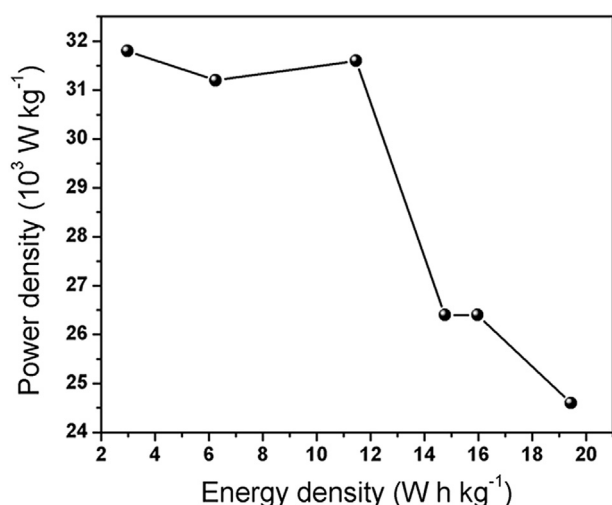
Fig. 8. Ragone plot of energy density vs. power density for NiO hollow spheres electrode.

supercapacitor applications. Also, the porous hollow sphere structure of ultrathin NiO nanosheets can be particularly beneficial in the transport of OH^- ions for good electrochemical performance and in maintaining structure rigidity for electrochemical stability during the charge–discharge cycling processes.

In comparison, as can be seen in the Ragone plot (Fig. 8), the current work has a higher power density (24.6 kW kg^{-1}) than the reported value (0.145–10 kW kg^{-1}) for supercapacitors in literature [58,59]. However, the specific energy density of 19.44 W h kg^{-1} (10 A g^{-1}) obtained in this work appears to be in the lower range of other supercapacitors (16.7–62 W h kg^{-1}) reported in literature [58,59].

6. Conclusions

In summary, porous hollow nanospheres (or spherical shells) made of NiO nanosheets have been synthesized and tested for their electrochemical performance. The material preparation involves a two-step activation procedure and the subsequent nucleation and growth by electroless deposition. The nanosized CPS cores, which were synthesized in our laboratory, are first sensitized with Sn^{2+} and subsequently activated with Pd to create catalyst sites. The catalyst sites created by this two-step activation process are further converted into nucleation sites upon which Ni is reduced and grown by electroless deposition to obtain a CPS@Ni core–shell composite nanoparticle. By calcination in air, the CPS core is eliminated and metallic Ni nanoshell is converted into NiO. The as-prepared hollow NiO nanospheres (or uncored nanoshells) were characterized by TEM, XRD and N$_2$-absorption measurements. Results show that the nanostructured hollow nanospheres are made of randomly oriented NiO nanosheets, forming a porous structure with a specific surface area of 81 m^2 g^{-1} and with a mesopore size range of 3–17 nm. The electrochemical characteristics of the electrodes made of these nanostructured NiO materials were determined by the CV and galvanostatic measurements. These electrochemical tests indicate that when used as electrodes for supercapacitors, the NiO nanosheet hollow spheres exhibit an improved reversible capacitance of 600 F g^{-1} after 1000 cycles at a high current density of 10 A g^{-1}. This suggests that these NiO nanosheet hollow spheres have a desired porous network for high energy density storage and an excellent electrochemical stability at a high rate. Energy density and power density of the nano-structured NiO materials under study are 19.44 W h kg^{-1} and

24.6 kW kg^{-1}. Analysis reveals that the good electrochemical performance of these electrodes is attributed to the improved OH^- transport in the porous network structures associated with the hollow spheres of randomly oriented NiO nanosheets.

References

[1] J. Li, E.H. Liu, W. Li, X.Y. Meng, S.T. Tan, J. Alloy Compd. 478 (2009) 371–374.
[2] L. Fan, L. Tang, H.F. Gong, Z.H. Yao, R. Guo, J. Mater. Chem. 22 (2012) 16376–16381.
[3] T.S. Hyun, H.L. Tuller, D.Y. Youn, H.G. Kim, I.D. Kim, J. Mater. Chem. 20 (2010) 9172–9179.
[4] P. Yu, X. Zhang, Y. Chen, Y.W. Ma, Z.P. Qi, Mater. Chem. Phys. 118 (2009) 303–307.
[5] S.J. Ding, T. Zhu, J.S. Chen, Z.Y. Wang, C.L. Yuan, X.W. Lou, J. Mater. Chem. 21 (2011) 6602–6606.
[6] H.L. Wang, H.S. Casalongue, Y.Y. Liang, H.J. Dai, J. Am. Chem. Soc. 132 (2010) 7472–7477.
[7] S.M. Dong, X.A. Chen, L. Gu, X.H. Zhou, H.X. Xu, H.B. Wang, Z.H. Liu, P.X. Han, J.H. Yao, L. Wang, G.L. Cui, L.Q. Chen, Appl. Mater. Interfaces 3 (2011) 93–98.
[8] T. Brezesinski, J. Wang, S.H. Tolbert, B. Dunn, Nat. Mater. 9 (2010) 146–151.
[9] T. Zhu, J.S. Chen, X.W. Lou, J. Mater. Chem. 20 (2010) 7015–7020.
[10] G. Wee, H.Z. Soh, Y.L. Cheah, S.G. Mhaisalkar, M. Srinivasan, J. Mater. Chem. 20 (2010) 6720–6725.
[11] X. Xia, J. Tu, Y. Zhang, J. Chen, X. Wang, C. Gu, C. Guan, J. Luo, H.J. Fan, Chem. Mater. 24 (2012) 3793–3799.
[12] Y.Q. Zhang, X.H. Xia, J.P. Tu, Y.J. Mai, S.J. Shi, X.L. Wang, C.D. Gu, J. Power Sources 199 (2012) 413–417.
[13] R.B. Moghaddam, P.G. Pickup, Phys. Chem. Chem. Phys. 12 (2010) 4733–4741.
[14] X. Zhao, C. Johnston, A. Crossley, P.S. Grant, J. Mater. Chem. 20 (2010) 7637–7644.
[15] K.W. Nam, W.S. Yoon, K.B. Kim, Electrochim. Acta 47 (2002) 3201–3209.
[16] S.L. Xiong, C.Z. Yuan, X.G. Zhang, Y.T. Qian, Crystengcomm 13 (2011) 626–632.
[17] Y.G. Wang, Y.Y. Xia, Electrochim. Acta 51 (2006) 3223–3227.
[18] X.J. Zhang, W.H. Shi, J.X. Zhu, W.Y. Zhao, J. Ma, S. Mhaisalkar, T.L. Maria, Y.H. Yang, H. Zhang, H.H. Hng, Q.Y. Yan, Nano Res. 3 (2010) 643–652.
[19] C. Ge, Z. Hou, B. He, F. Zeng, J. Cao, Y. Liu, Y. Kuang, J. Sol-Gel Sci. Technol. 63 (2012) 146–152.
[20] M. Wu, Y. Huang, J. Jow, W. Yang, C. Hsieh, H. Tsai, Int. J. Hydrogen Energy 33 (2008) 2921–2926.
[21] U.M. Patil, R.R. Salunkhe, K.V. Gurav, C.D. Lokhande, Appl. Surf. Sci. 255 (2008) 2603–2607.
[22] D. Wang, Q. Wang, T. Wang, Ionics 19 (3) (March 2013) 559–570.
[23] X.F. Song, L. Gao, J. Phys. Chem. C 112 (2008) 15299–15305.
[24] X. Sun, J. Liu, Y. Li, Chem. Eur. J. 12 (2005) 2039–2047.
[25] W.Z. Wang, Y.K. Liu, C.K. Xu, C.L. Zheng, G.H. Wang, Chem. Phys. Lett. 362 (2002) 119–122.
[26] H.J. Liu, T.Y. Peng, D.E. Zhao, K. Dai, Z.H. Peng, Mater. Chem. Phys. 87 (2004) 81–86.
[27] D.S. Wang, R. Xu, X. Wang, Y.D. Li, Nanotechnology 17 (2006) 979–983.
[28] Q. Yang, J. Sha, X.Y. Ma, D.R. Yang, Mater. Lett. 59 (2005) 1967–1970.
[29] Q.X. Xia, K.S. Hui, K.N. Hui, D.H. Hwang, S.K. Lee, W. Zhou, Y.R. Cho, S.H. Kwon, Q.M. Wang, Y.G. Son, Mater. Lett. 69 (2012) 69–71.
[30] C.Z. Yuan, X.G. Zhang, L.H. Su, B. Gao, L.F. Shen, J. Mater. Chem. 19 (2009) 5772–5777.
[31] J.W. Lang, L.B. Kong, W.J. Wu, Y.C. Luo, L. Kang, Chem. Commun. (2008) 4213–4215.
[32] H. Dong, S.Y. Lee, G.R. Yi, Macromol. Res. 17 (2009) 397–402.
[33] U. Lee, J.S. Oh, P.C. Lee, D.O. Kim, Y. Lee, J. Nam, J. Electron. Mater. 37 (2008) 1648–1652.
[34] J. Gao, F. Tang, J. Ren, Surf. Coat. Tech. 200 (2005) 2249–2252.
[35] X. Yang, Q.B. Li, H.X. Wang, J.L. Huang, L.Q. Lin, W.T. Wang, D.H. Sun, Y.B. Su, J.B. Opiyo, L.W. Hong, Y.P. Wang, N. He, L.S. Jia, J. Nanoparticle Res. 12 (2010) 1589–1598.
[36] S. Papp, I. Dekany, Colloid Polym. Sci. 284 (2006) 1049–1056.
[37] Y.H. Ma, Q.H. Zhang, Appl. Surf. Sci. 258 (2012) 7774–7780.
[38] Q. Zhang, M. Wu, M. Zhao, Surf. Coat. Technol. 192 (2005) 213–219.
[39] J. Jiang, H. Lu, L. Zhang, N. Xu, Surf. Coat. Technol. 201 (2007) 7174–7179.
[40] H. Guo, Z. Qin, J. Wei, C. Qin, Surf. Coat. Technol. 200 (2005) 2531–2536.
[41] P. Tierno, W.A. Goedel, J. Phys. Chem. B 110 (2006) 3043–3050.
[42] M. Kruk, M. Jaroniec, Chem. Mater. 13 (2001) 3169–3183.

[43] P. Lin, Q.J. She, B.L. Hong, X. Liu, Y.N. Shi, Z. Shi, M.S. Zheng, Q.F. Dong, J. Electrochem. Soc. 157 (2010) A818—A823.
[44] P.A. Nelson, J.R. Owen, J. Electrochem. Soc. 150 (2003) A1313—A1317.
[45] K.W. Nam, E.S. Lee, J.H. Kim, Y.H. Lee, K.B. Kim, J. Electrochem. Soc. 152 (2005) A2123—A2129.
[46] I. Bouessay, A. Rougier, J.M. Tarascon, J. Electrochem. Soc. 151 (2004) H145—H152.
[47] K.W. Nam, K.H. Kim, E.S. Lee, W.S. Yoon, X.Q. Yang, K.B. Ki, J. Power Sources 182 (2008) 642—652.
[48] P. Delichere, S. Joiret, A. Hugot-le Goff, K. Bange, B. Hetz, J. Electrochem. Soc. 135 (1988) 1856—1857.
[49] B.E. Conway, V. Birss, J. Wojtowicz, J. Power Sources 66 (1997) 1—14.
[50] B.E. Conway, J. Electrochem. Soc. 138 (1991) 1539—1548.
[51] A.J. Bard, L.R. Faulkner, Electrochemical Methods: Fundamentals and Applications, second ed., John Wiley & Sons, 2000.
[52] S.K. Meher, P. Justin, G.R. Rao, Nanoscale 3 (2011) 683—692.
[53] J.P. Zheng, Electrochem. Solid-State Lett. 2 (1999) 359—361.
[54] T. Liu, W.G. Pell, B.E. Conway, S.L. Roberson, J. Electrochem. Soc. 145 (1998) 1882—1888.
[55] J. Chun, J.H. Chun, Developments in Electrochemistry, InTech, Croatia, 2012, pp. 3—27.
[56] D.A. Harrington, B.E. Conway, Electrochim. Acta 32 (1987) 1703—1712.
[57] V. Srinivasan, J.W. Weidner, J. Electrochem. Soc. 147 (2000) 880—885.
[58] H. Jiang, T. Sun, C.Z. Li, J. Ma, RSC Adv. 1 (2011) 954—957.
[59] Q. Lu, M.W. Lattanzi, Y.P. Chen, X.M. Kou, W.F. Li, X. Fan, K.M. Unruh, J. Chen, J.Q. Xiao, Angew. Chem. Int. Ed. 50 (2011) 6847—6850.